Advanced Water-Gas Shift Membrane Reactor

Final Technical Report

Project Period:	1 July 2005 to 30 June 2007
Date of Report:	September 2007
Award Number:	DE-FG26-05NT42453
Authors:	Sean C. Emerson (Primary Contact) Thomas H. Vanderspurt (Principle Investigator) Susanne Opalka Rakesh Radhakrishnan Rhonda Willigan
Submitting Organization:	United Technologies Research Center 411 Silver Lane East Hartford, CT 06108
Working Partners:	Metal Hydride Technologies Incorporated QuesTek Innovations LLC

DE-FG26-05NT42453
United Technologies Research Center

DE-FG26-05NT42453
United Technologies Research Center

Abstract

The overall objectives for this project were: (1) to identify a suitable PdCu tri-metallic alloy membrane with high stability and commercially relevant hydrogen permeation in the presence of trace amounts of carbon monoxide and sulfur; and (2) to identify and synthesize a water gas shift catalyst with a high operating life that is sulfur and chlorine tolerant at low concentrations of these impurities. This work successfully achieved the first project objective to identify a suitable PdCu tri-metallic alloy membrane composition, $Pd_{0.47}Cu_{0.52}G5_{0.01}$, that was selected based on atomistic and thermodynamic modeling alone. The second objective was partially successful in that catalysts were identified and evaluated that can withstand sulfur in high concentrations and at high pressures, but a long operating life was not achieved at the end of the project. From the limited durability testing it appears that the best catalyst, Pt-Re/$Ce_{0.333}Zr_{0.333}E4_{0.333}O_{2}$, is unable to maintain a long operating life at space velocities of 200,000 h^{-1}. The reasons for the low durability do not appear to be related to the high concentrations of H_2S, but rather due to the high operating pressure and the influence the pressure has on the WGS reaction at this space velocity.

Contents

1 Executive Summary

The overall objectives for this project were: (1) to identify a suitable PdCu tri-metallic alloy membrane with high stability and commercially relevant hydrogen permeation in the presence of trace amounts of carbon monoxide and sulfur; and (2) to identify and synthesize a water gas shift catalyst with a high operating life that is sulfur and chlorine tolerant at low concentrations of these impurities. This work successfully achieved the first project objective to identify a suitable PdCu tri-metallic alloy membrane with high stability and commercially relevant hydrogen permeation in the presence of trace amounts of carbon monoxide and sulfur. A promising alloy composition, $Pd_{0.47}Cu_{0.52}G5_{0.01}$, was selected based on atomistic and thermodynamic modeling alone. To achieve the DOE's goals of identifying a suitable Pd alloy membrane that can withstand the challenges of coal gasifier syngas, this alloy's performance needs to be verified experimentally. The construction and experimental study of a membrane separator based on this alloy is planned as part of another project for the DOE, DE-FC26-07NT43055.

The second objective was partially successful in that catalysts were identified and evaluated that can withstand sulfur in high concentrations and at high pressures, but a long operating life was not achieved at the end of the project. From the limited durability testing it appears that the best catalyst, Pt-Re/$Ce_{0.333}Zr_{0.333}E4_{0.333}O_2$, is unable to maintain a long operating life at space velocities of 200,000 h^{-1}. The reasons for the low durability do not appear to be related to the high concentrations of H_2S, but rather due to the high operating pressure and the influence the pressure has on the WGS reaction. Additional work should be performed to investigate the causes of catalyst deactivation at high pressures as well as to estimate the amount of catalyst required to maintain life for DOE's coal gasification applications.

2 Results

2.1 Hydrogen Separation Membrane Alloy

A combination of atomic simulations, experimental measurements and thermodynamic assessments were used to virtually formulate a new high H permeability ternary Pd-Cu-G5 alloy composition for advanced WGS membrane reactors with improved thermal stability and chemical resistance, where G5 is the ternary transition metal element. The alloy development was accomplished by three modeling stages: (a) the virtual screening and down-selection of ternary transition metal (TM) substituents for the Pd-Cu B2 phase, (b) the benchmarking of Pd-Cu and Pd-Cu-H property predictions, and (c) the virtual extension to Pd-Cu-TM and Pd-Cu-TM-H property predictions.

In the first stage, the bulk stability, slab surface energy and reactivity with O and S species were simulated for the PdCu B2 phases substituted with six TM candidates. In addition, atomic simulations and thermodynamic assessments were made to evaluate relevant competitive hydride and intermetallic phases that could be formed with the six TM candidates. These screening results were used to create a knowledge base to guide the down-selection of two TM candidates, J6 and G5, with the best substitution stability,

lowest substituted surface reactivity, and lowest raw material cost. This report will highlight the ternary alloy development conducted in the later two stages of this program.

In the second stage, rigorous thermodynamic assessments of the Pd-Cu and Pd-Cu-H were made from experimental measurements, including new H solubility measurements within the Pd-Cu B2 phase region, and supplemental atomic modeling. The assessments enabled modeling of H solubility over a wide range of T, P and composition conditions. First-principles lattice dynamics predictions were used to simulate H diffusivity in the PdCu B2 lattice. The H solubility modeling and H diffusivity predictions were combined to successfully validate our capability to predict H permeability in the PdCu B2 system.

The third stage modeled the impact of the J6 and G5 substitution in the PdCu B2 region on stability and H permeability. Atomic simulations of binary and ternary substituted phases enabled ternary thermodynamic assessments of the uncharacterized Pd-Cu-J6 and Pd-Cu-G5, which delineated the more soluble G5 substituent for final alloy down-selection. Following the second stage protocol, atomic simulations were made to enable thermodynamic assessment of H solubility and the prediction of H diffusivity in the Pd-Cu-G5 system. Finally, simulations were made to evaluate relative surface reactivities with key AWGSMR gas species. The outcome was the identification of a promising new alloy composition, $Pd_{0.47}Cu_{0.52}G5_{0.01}$, predicted to have higher phase stability to thermal and compositional fluctuations likely to occur during AWGSMR operation, with high H permeability and resistance to S impurities.

2.1.1 Thermodynamic Assessment of the Pd-Cu-H Ternary System

Baseline thermodynamic assessments were developed for the Pd-Cu, Pd-H, and Cu-H binary and Pd-Cu-H ternary systems to prepare for the virtual design of the ternary Pd-Cu-TM alloys [1-2]. A thermodynamic description of the Pd-Cu system, including the ordered B2 phase, was established, and the calculated phase diagram is shown in Figure 1. In order to validate the first principles predictive capabilities, predicted ordered B2 and FCC-type Pd-Cu alloy finite temperature thermodynamic properties were shown to have acceptable agreement with the thermodynamic modeling.

The Pd-Cu-H system has no ternary compounds. The ternary interaction parameters of the fcc and B2 phase were evaluated from H desorption isotherm, fcc para-equilibrium miscibility gap boundaries, and partial H enthalpy measurements. The newly measured H solubilities in B2 and fcc for the $Pd_{0.44}Cu_{0.56}$ composition from 100-200 ºC are shown in Figure 2. First principles predicted end member thermodynamic properties of bcc-Cu, bcc-Pd, and B2-PdCu with the tetrahedral interstitial sites completely filled with H were also used. The ternary Pd-Cu-H isothermal section at 473 K and 10 bar is shown in Figure 3. The H solubility at 673 K over a range of pressures, up to 43.8bar, is shown in Figure 4.

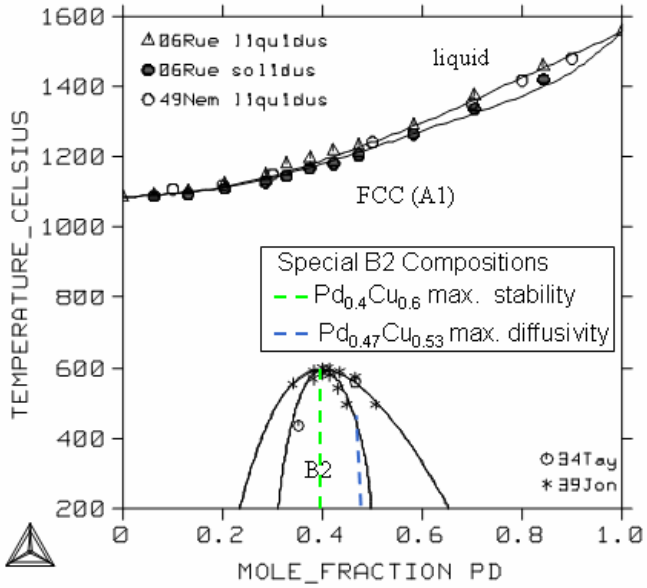

Figure 1: Pd-Cu phase diagram developed by thermodynamic modeling.

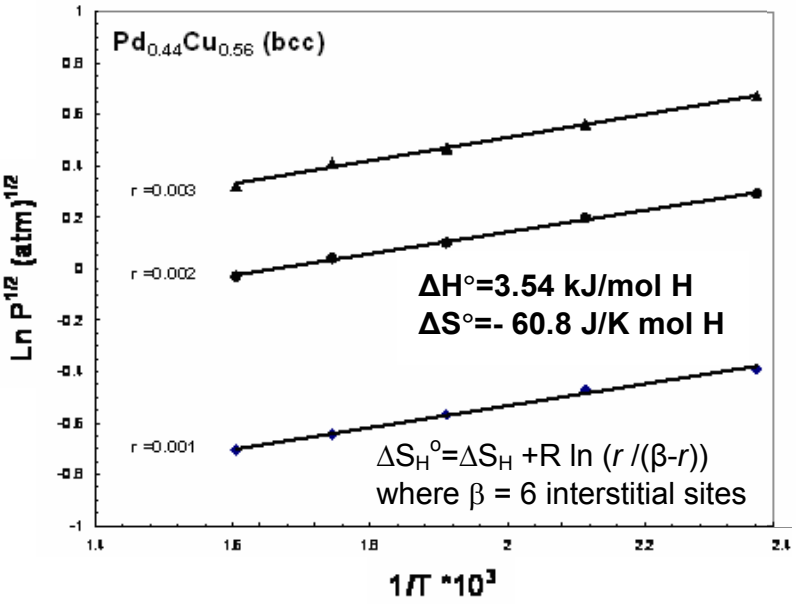

Figure 2: Van't Hoff plot determined for dilute regime H solubility measurements in $Pd_{0.44}Cu_{0.56}$ B2 alloy using a Sievert's apparatus.

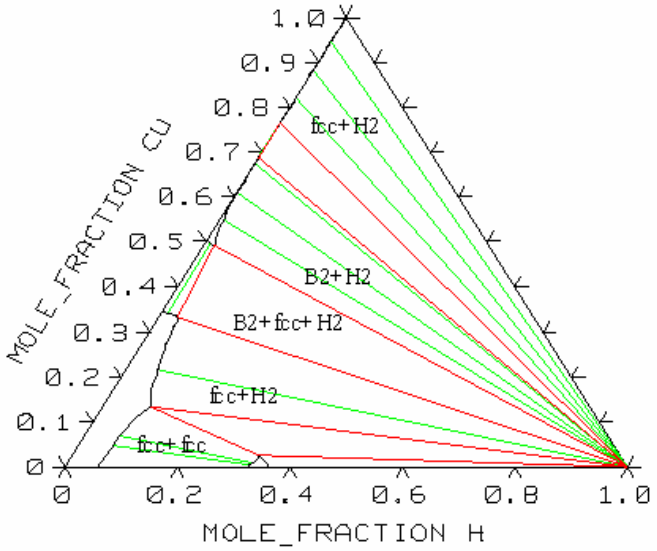

Figure 3: Calculated Pd-Cu-H isothermal section at 473 K and 10 atm, showing the small H solubility in the B2-PdCu composition range.

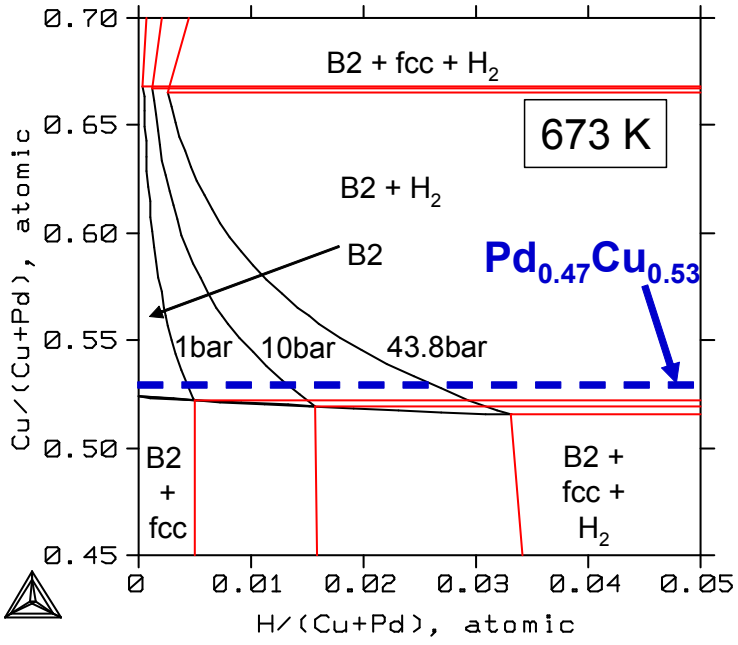

Figure 4- Calculated H solubility in the PdCu B2 phase at 673 K (400 ºC) over a range of pressures, up to 43.8 bar (WGS reactor operating conditions).

2.1.2 Simulations of H Diffusion Behavior in the Ordered PdCu B2 Phase

Atomic simulations of hydrogen solubility and diffusion behavior were made on an interstitial hydrogen atom in a 2×2×2 supercell of the ordered $Pd_{0.5}Cu_{0.5}$ B2 phase. The atomic lattice was fixed and only ionic relaxation was allowed to predict the limiting fast diffusion conditions of a dilute H concentration at high reactor operating temperatures. The tetrahedral site, bounded by 2 Pd and 2 Cu atoms was indeed found to be slightly more energetically more favorable than the octahedral site bounded by 4 Pd and 2 Cu atoms. Direct method lattice dynamic calculations were made to determine zero point energy (ZPE) corrections to the interstitial and transition state, and to confirm the identity of the transition state. The ZPE-corrected activation barrier, $[\Delta H_{act} + \Delta ZPE_H]$, for diffusion from tetrahedral to tetrahedral site within a frozen atomic lattice was determined to be 6.96 kJ/mole. Using the quantum-corrected diffusion equation [3]

$$D = [n\,\alpha^2\,\kappa_B T / 6h]\,\exp\,[-\Delta H_{act} + \Delta ZPE_H / \kappa_B T] \qquad (1)$$

where n is the geometrical jump factor, α is the tetrahedral-to-tetrahedral jump length of 1.5 Å, κ_B is Boltzmann's constant, and h is Planck's constant, a preexponential factor, D_0, of 2.1×10^{-7} m^2s^{-1} and a diffusivity of 6.3×10^{-8} m^2s^{-1} was determined at 673 K (400ºC). The predicted diffusivity for the ordered $Pd_{0.5}Cu_{0.5}$ B2 phase is compared to experimental data in Figure 5.

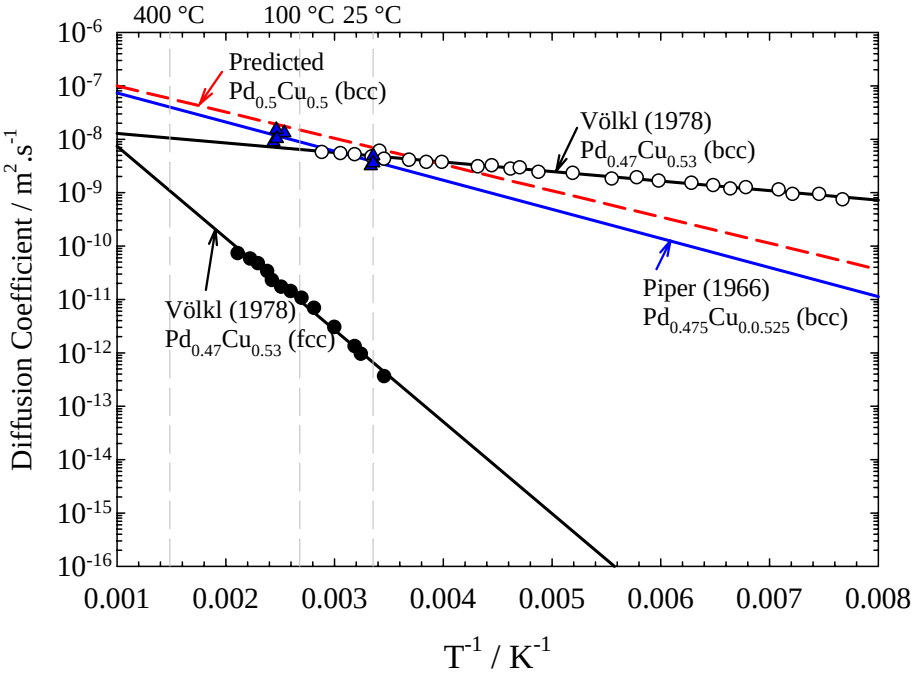

Figure 5: Comparison of predicted H diffusion coefficients for $Pd_{0.5}Cu_{0.5}$ to literature $Pd_{0.47}Cu_{0.53}$ experimental data from Piper [4] and Völkl [5].

2.1.3 Ternary Pd-Cu-TM Systems

First principles atomic predictions and thermodynamic modeling were combined to virtually design hydrogen-selective membrane ternary alloy Pd-Cu-TM compositions, formed by substituting one of the two down-selected TM alloying elements, G5 and J6, in Pd-Cu B2 alloy compositions. First principles predictions were made of these phases related to these two ternary systems. Atomic simulations were also made to mechanistically investigate hydrogen interactions in the ternary alloy phases. Thermodynamic assessments of experimental and predicted thermodynamic data were conducted to model the TM alloying element solubility limits in the PdCu B2 phase region in order to establish recommended alloy composition ranges for further experimental investigation. Thermodynamic modeling of the hydrogen solubility in the respective B2 ternary alloy phases was used to target specific alloy compositions with enhanced hydrogen solubility, which could lead to increased hydrogen permeability.

The thermodynamic descriptions of the Pd-Cu-G5 and Pd-Cu-J6 ternary systems were developed by combining the constituent binary thermodynamic descriptions with ternary B2 phase interaction parameters. The latter were estimated from atomic simulated TM substitution energies for Cu in both the high H permeability $Pd_{0.5}Cu_{0.5}$ and the high stability $Pd_{0.375}Cu_{0.625}$ ordered B2 alloy phases. Each TM substitution level was represented by one or more high symmetry ordered structures. This approach enabled the investigation of a range of nearest neighbor and next-nearest neighbor combinations, and could conceivably be used to derive a random substitution energy function without requiring the simulation of a large number of configurations. The lowest energy structure at each substitution level was selected for first principles thermodynamic predictions and the thermodynamic assessments. The enthalpies of formation for the B2 alloys decreased favorably with increasing G5 substitution in the $Pd_{0.5}Cu_{0.5}$ phase. In all other cases, the enthalpies of formation increased with increasing TM substitution, indicating very low TM solubility. The ternary isopleths indicating the solubilities of G5 and J6 in the PdCu system is shown in Figure 6. G5 has a higher solubility of approximately 1.5 atomic % in the $Pd_{0.47}Cu_{0.53}$ composition. The G5 solubility is limited by the high stability predicted for the competing Pd_2G5 lower order phase. The maximum J6 solubility is very low (2×10^{-2} atomic %), due to the unilateral endothermic mixing interactions with the PdCu B2 lattice.

2.1.4 $Pd_{0.50}Cu_{0.44}G5_{0.06}$ Studies

Since G5 showed the maximum solubility of 1.5 atomic percent in the B2 phase close to PdCu composition and G5 is predicted to more favorably substitute on the Cu sublattice, the optimum Pd-Cu-G5 composition was approximated with the $Pd_{0.50}Cu_{0.44}G5_{0.06}$ (Pd_8Cu_7G5) composition in the first principles modeling. This modeling enabled the predictive comparison of Pd-Cu-G5 alloy H_2S interactions and H permeability with that of the high diffusivity $Pd_{0.47}Cu_{0.53}$ B2 alloy, where the latter composition was represented as the PdCu B2 phase.

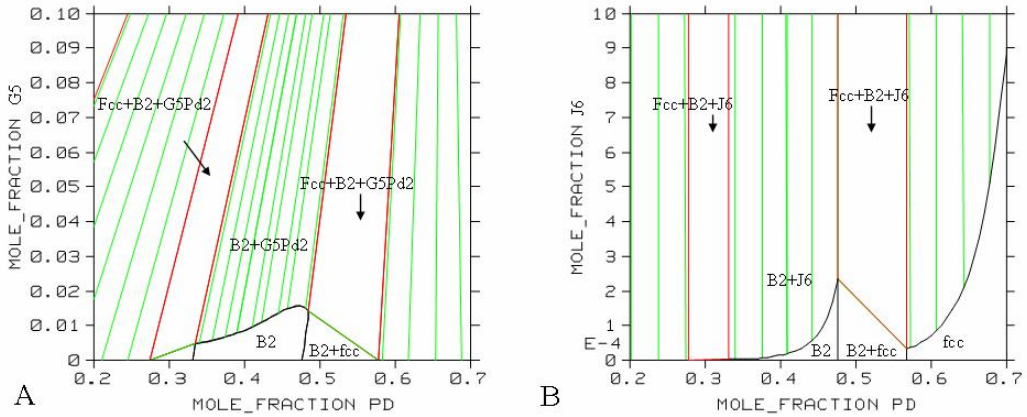

Figure 6: Ternary isopleths showing A G5 and B) J6 solubility in Pd-Cu binary system at 400 °C determined from thermodynamic modeling.

2.1.4.1 Hydrogen interactions with the Pd-Cu-TM alloys

Interstitial H behavior in the slightly expanded Pd_8Cu_7G5 lattice was significantly altered compared to the PdCu B2 phase, where the equivalent Pd_8Cu_7G5 unit cell lattice parameter was 0.03 Å larger than that of PdCu B2. In order to realistically represent a more dilute concentration regime, the atomic lattices were fixed and only ionic relaxation was allowed during ground state simulations with 6 atomic% interstitial H substitutions. In spite of the larger Pd_8Cu_7G5 interatomic distances, calculations indicate that the H was not stable in the interstitial positions adjacent to the G5 substituent atom and migrated to nearby interstitial sites bordered by Pd and Cu atoms. The substitution energies for the stable interstitial sites within the Pd_8Cu_7G5 lattice are more endothermic compared to that determined for the PdCu B2 phase, as shown in Table 1.

Table 1: Ground state enthalpies for 6 atomic% H substitution in Pd_8Cu_7G5 and PdCu B2 ordered phases in most stable interstitial sites.

Composition	Interstitial Site	H substitution Enthalpy (kJ/mole H)
Pd_8Cu_7G5 B2	Tetrahedral	22.62
Pd_8Cu_7G5 B2	Octahedral	23.93
PdCu B2	Tetrahedral	3.93

The most stable Pd_2Cu_2 tetrahedral and the slightly off-center Pd_4Cu_2 octahedral H interstitial sites in Pd_8Cu_7G5 were very close in energy. The two possible tetrahedral-to-octahedral and tetrahedral-to-tetrahedral diffusion pathways were modeled by identifying favorable transition state sites close to the Pd_2Cu triangular face centers between the most stable interstitial sites. The PdCu B2 phase ΔZPE_H correction determined for H tetrahedral-to-tetrahedral diffusion was used to correct the diffusion activation enthalpies, ΔH_{act},

listed in Table 2. Hydrogen diffusion in the Pd_8Cu_7G5 composition was modeled weighting the diffusion among the two pathways by the relative distribution of the octahedral and tetrahedral sites in the PdCu B2 lattice. There are 3 octahedral sites and 6 tetrahedral sites per atom in the B2 body centered cubic lattice, so that the weighting was 3/9 for tetrahedral-to-octahedral diffusion and 6/9 for tetrahedral-to-tetrahedral diffusion. The equation for quantum-corrected bimodal diffusion over both of these pathways in Pd_8Cu_7G5, was derived by modifying the single-mode equation, given in Equation. (1)

$$D\ (\mathrm{m^2/s}) = 1/3*[\ n\ \alpha^2\ \kappa_B T / 6h\ ]\ \exp\ [-\Delta H_{\text{act oct-tet}} + \Delta ZPE_H / \kappa_B T\ ] + 2/3*[n\ \alpha^2\ \kappa_B T / 6h]\ \exp\ [-\Delta H_{\text{act tet-tet}} + \Delta ZPE_H / \kappa_B T\ ] \quad (2)$$

where n is the geometrical jump factor set at 0.667, α is the jump length in m between interstitial sites given in Table 2. Using this relationship, a diffusivity of 9.69×10^{-09} m^2/s was determined at 673 K (400ºC) for the Pd_8Cu_7G5 B2 ordered phase.

Table 1: Predicted diffusion parameters in Pd_8Cu_7G5 and PdCu B2 ordered phases.

Composition	Diffusion Pathway	($\Delta H_{act} + \Delta ZPE_H$) (kJ/mole H)	Jump Length, α m
Pd_8Cu_7G5 B2	Tetrahedral-to-Tetrahedral	5.05	1.4E-10
Pd_8Cu_7G5 B2	Tetrahedral-to-Octahedral	16.33	1.0E-10
PdCu B2	Tetrahedral-to-Tetrahedral	6.96	1.5E-10

2.1.4.2 Ternary Pd-G5-H and Cu-G5-H and quaternary Pd-Cu-G5-H systems

In addition to the previously reported Pd-Cu-Tm and Pd-Cu-H ternary assessments [5], assessments were made of the Pd-G5-H and Cu-G5-H ternary systems, to set the stage for development of the Pd-Cu-G5-H system assessment. H interaction parameters were developed from first principles thermodynamic predictions made of the hypothetical PdG5, PdG5H, CuG5 and CuG5H B2 phases. These parameters were used to predict H solubility in $Pd_{(0.99-x)}Cu_xG5_{0.01}$ compositions at 673 K (400 ºC) and a range of different pressures, as shown in Figure 7. Compared to the PdCu-B2 alloy, the addition of 1 atomic % G5 expands the B2 stability region to a slightly higher Pd content (about 1 atomic % Pd), on the Pd-rich side. Thus, G5 addition is shown to stabilize the highest diffusivity $Pd_{0.47}Cu_{0.53}$ composition against decomposition into a two phase B2+fcc structure in the adjacent phase region. Figure 7 also shows that the G5 addition does not have a significant impact on H solubility in the B2 alloy, as compared to Figure 4.

2.1.4.3 Hydrogen Permeability Predictions

The prediction of the ideal bulk H permeability, Q (in units of mol s^{-1} m^{-1} $Pa^{-0.5}$), the product of solubility and diffusivity for a given alloy, enables the quantitative evaluation of surface contributions in experimental permeability data. In a one-dimensional membrane mass transfer model, the H flux, J_{H2}, is given by

$$J_{H2} = (Q/\ l\ )\ (p_1^{\ 0.5} - p_2^{\ 0.5}) = (D\ /\ l\ )(C_1 - C_2) \quad (3)$$

where l is the membrane thickness, p_1 and p_2 are the H_2 partial pressures above the membrane surface, C_1 and C_2 are the surface soluble H concentrations in mol/m^3, and where the subscripts 1 and 2 refer to the retentate and permeate sides of the membrane [6]. The surface H concentration C is proportional to the H/metal ratio, n, by κ, a conversion factor (in units of mol H/m^3) corresponding to the lattice volume when n=1, where n is proportional to the square root of pressure, $p^{0.5}$, by Sievert's constant, K_s. Using these relationships, J_{H2} can be expressed as

$$J_{H2} = (D\,\kappa K_s)(l)^{-1}(p_1^{0.5} - p_2^{0.5}) \quad (4)$$

The solubility can therefore be determined from the product [κK_s]. The kappa conversion factor, κ, for the lattice volume when n=1, was estimated from the $Pd_{0.47}Cu_{0.53}$ lattice and the established H partial molar volume increase relationship for Pd alloys [7], to be 1.0×10^5 mol H/m^3. Hydrogen solubility in $Pd_{0.47}Cu_{0.53}$ and $Pd_{0.47}Cu_{0.52}G5_{0.01}$ was calculated from the thermodynamic assessment modeling, where the Sievert's coefficient, K_s, was determined from the inverse slope of the square root of H_2 pressure versus the solublized H/metal ratio. The calculated solubility plot for $Pd_{0.47}Cu_{0.53}$ at 673 K is shown in Figure 8, where K_s was determined to be 1.25×10^{-5} Pa$^{-0.5}$. The calculated solubility plot for $Pd_{0.47}Cu_{0.52}G5_{0.01}$ at 673 K is shown in Figure 9, where K_s was determined to be 1.17×10^{-5} Pa$^{-0.5}$.

Using the first principles calculated diffusivity, the estimated κ conversion factor, and the K_s Sievert's coefficient from the thermodynamic assessments, the theoretical H bulk permeability, Q, was estimated to be 7.89×10^{-8} mol s^{-1} m^{-1} Pa$^{-0.5}$ in $Pd_{0.47}Cu_{0.53}$ and 1.11×10^{-8} mol s^{-1} m^{-1} Pa$^{-0.5}$ in $Pd_{0.47}Cu_{0.52}G5_{0.01}$ at 673 K. Practical necessity required that first principles diffusivity calculations be based on a $Pd_{0.5}Cu_{0.44}G5_{0.06}$ composition. Most experimental $Pd_{0.47}Cu_{0.53}$ membrane results are reported in terms of permeance for membranes of varying thickness and configuration, making direct comparison difficult. Our predicted permeability is more than an order magnitude larger than the permeabilities predicted and measured by Kamakoti et al. [8], however, it is consistent with the Ma *et al.* [9] H permeability of the $Pd_{0.47}Cu_{0.53}$ B2 phase being 1.1 times that of Pd at 623 K. The predicted permeabilities calculations and related parameters are summarized in Table 3.

Table 3: H solubility parameters, H diffusivity and permeability predictions for $Pd_{0.47}Cu_{0.52}G5_{0.01}$ and $Pd_{0.47}Cu_{0.53}$ ordered phases under advanced water gas shift membrane reactor conditions of 673 K (400 ºC) and 43.8 bar.

Composition	H Solubility K_s Pa$^{0.5}$	Conversion factor κ mol H/m^3	Diffusivity D m^2/s	Permeability Q mol s^{-1} m^{-1} Pa$^{-0.5}$
$Pd_{0.47}Cu_{0.52}G5_{0.01}$	1.17E-05	9.78E+04	9.69E-09	1.11E-08
$Pd_{0.47}Cu_{0.53}$	1.25E-05	1.00E+05	6.30E-08	7.89E-08

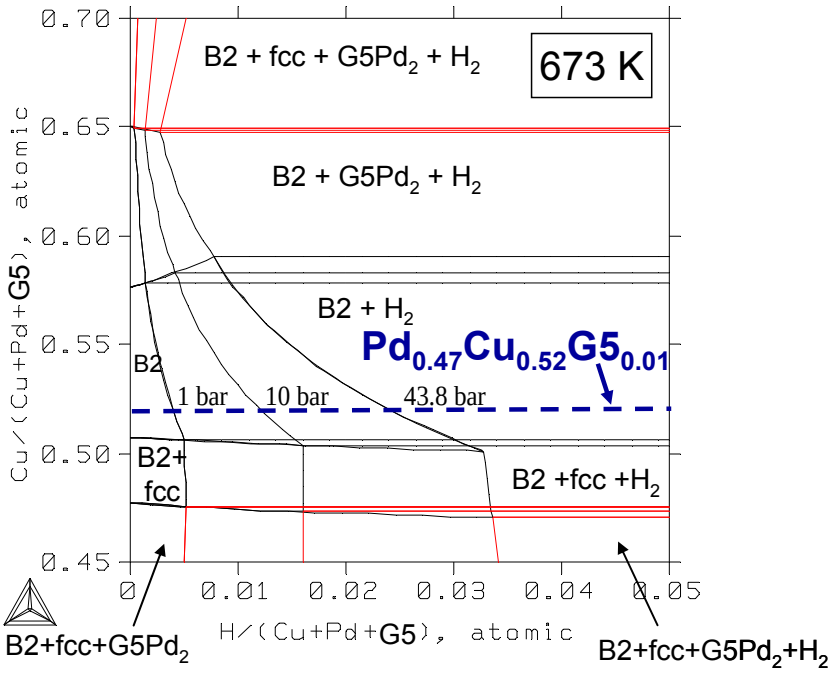

Figure 7: The calculated H solubility in the $Pd_{(0.99-x)}Cu_xG5_{0.01}$ alloy at 673 K (400 ºC) and at a range of pressures.

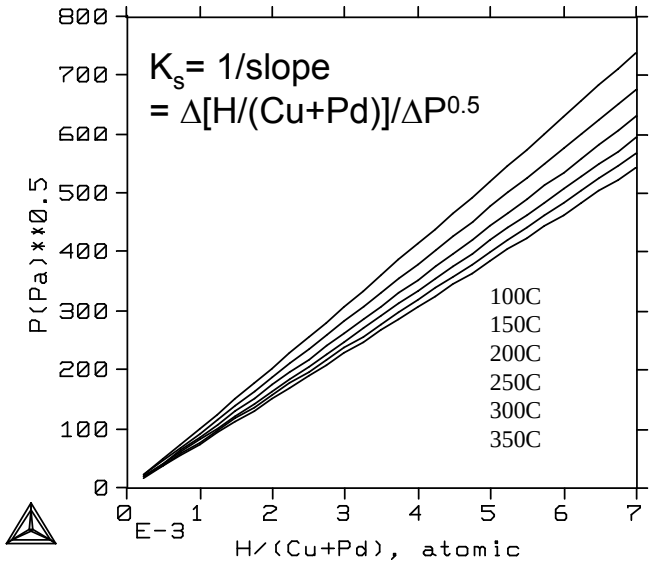

Figure 8: The Sievert's solubility predictions for the $Pd_{0.47}Cu_{0.53}$ B2 alloy.

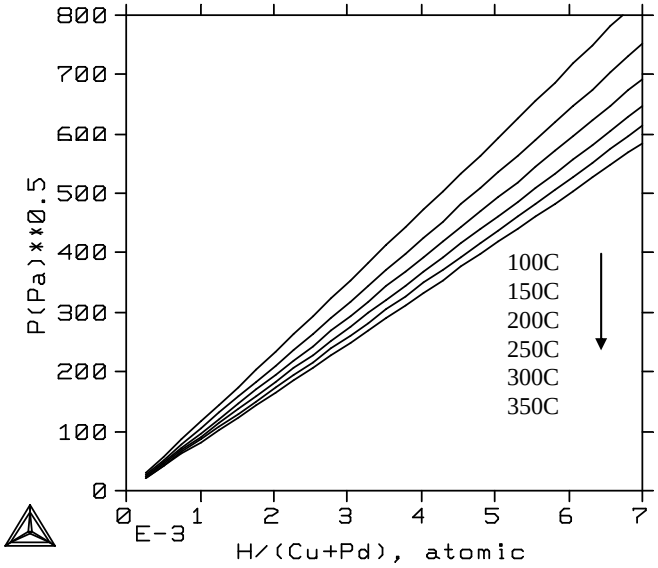

Figure 9: The Sievert's solubility predictions for the $Pd_{0.47}Cu_{0.52}G5_{0.01}$ B2 alloy.

2.1.4.4 Surface Adsorbate Interactions

Ground state minimizations were made to profile the interactions of varying adsorption coverages of H_2, H_2S, and CO molecules on a 32 atom, 4 layer periodic PdCu (110) surface, in order to benchmark competitive surface adsorption mechanisms. In the most stable relaxed ground state adsorption configuration, one H_2 molecule on a 4x4 PdCu (110) slab [0.25 monolayer (ML)] adsorbed 1.9 Å above a surface Pd atom with the molecular axis parallel to the surface, binding with a -28.64 kJ/mol per H_2 modest favorable electronic adsorption enthalpy. In the full H_2 monolayer, the electronic adsorption enthalpy weakened to -21.4 kJ/mol per H_2 and the H_2 molecules oriented towards the nearest neighbor subsurface Pd atoms. Carbon monoxide adsorption on top of Pd was predicted to be very stable with an adsorption enthalpy of -124.6 kJ/mol, and most likely contributes to the blocking of active H adsorption sites. In the most favorable relaxed 0.25 ML H_2S configuration, the S atom adsorbed 2.4 Å above a surface Pd atom with the molecular plane tilted 16º away from the surface plane with an adsorption enthalpy of -70.9 kJ/mol, in good agreement with previous work [10]. In the 1.0 ML adsorbed H_2S configuration, the H_2S molecules rotated alternately in opposite directions to minimize repulsion and facilitate hydrogen-bonding with a significantly weaker adsorption enthalpy. Repulsive interactions at high ML fractions could facilitate H_2S dissociative adsorption, leading to sulfur surface poisoning shown to be very favorable by atomic simulations [11]. The adsorption of H_2 and H_2S on adjacent surface Pd atoms had a combined weaker adsorption enthalpy of -77.2 kJ/mol, due to the poisoning interactions of the adsorbed H_2S. Finite temperature surface energy predictions were made for H_2 and H_2S partial

pressures of 2×10^{-2} and 3×10^{-6} bar, respectively, and are shown in Figure 10. The predictions showed that at these partial pressures, the physisorption of up to 0.5 ML H_2 would be favorable at the 673 K reactor operating temperature without the interference of H_2S site blocking. Hydrogen sulfide was predicted to only remain physisorbed in a 0.25 ML coverage up to 430 K. These predictions do not take the contributions from irreversible H_2S dissociative adsorption into account. However increasing the H_2 partial pressure should decrease metal sulfidation.

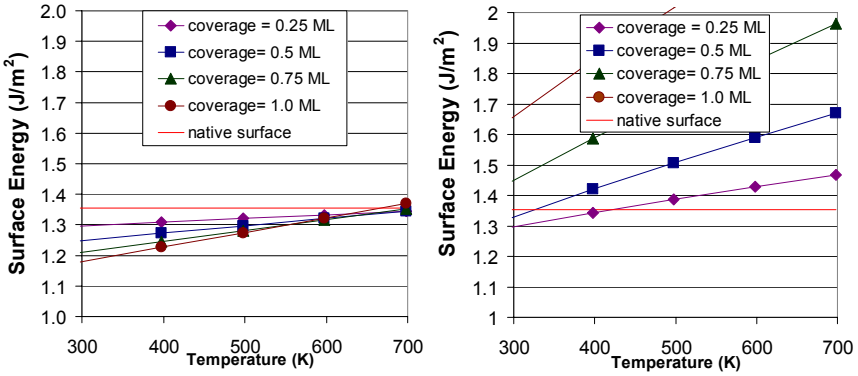

Figure 10: Finite temperature surface energy predictions for coal feed gas pressure conditions: a) H_2 adsorption at 2 x 10^{-2} bar H_2 pressure and b) H_2S adsorption at 3 x 10^{-6} bar H_2S pressure.

Simulations were made to access the relative adsorption enthalpies of different molecular adsorbates on the lowest energy 32 atom, 4layer Pd_8Cu_7G5 (110) surface for comparison to the PdCu (110) surface. Although our previous simulations determined that the G5 substituent was more stable in the subsurface, adsorption simulations surveyed both slabs with G5 at the surface and with G5 in the subsurface layer. The molecular adsorption energies on the PdCu and Pd_8Cu_7G5 B2 (110) surfaces are compared in Table 4. The H_2 adsorption interactions had weaker binding compared to the PdCu B2 alloy, especially on the Pd atom adjacent to G5. The CO adsorption enthalpy was significantly weaker over a number of surface sites. The adsorption of H_2S was significantly affected by the proximity of the G5 substituent. Hydrogen sulfide dissociated in interaction with G5 at the surface, resulting in SH adsorbed on top of G5 and H adsorbed at a nearby quasi Pd_2Cu 3-fold site. Hydrogen sulfide adsorbed more weakly when G5 was in the subsurface, and a subsurface location for the refractory G5 element is energetically favorable in the PdCuG5 alloy. Thus as long as G5 remains in the subsurface, all adsorbate interactions are weakened. While prolonged exposure to conditions of low H_2 and high sulfur species partial pressures could lead to sulfidation and membrane damage, the membrane should be stable and effective for the selective separation of H_2 from H_2S containing reformate under the projected conditions of use. This prediction should be validated experimentally.

Table 4: Ground state electronic adsorption enthalpies, ΔH_{ADS}, of 0.25 monolayers of H_2, H_2S and CO on PdCu and Pd_8Cu_7G5 (110) 32 atom 4 layer slabs.

Composition	$\Delta H_{ADS\ H2}$ kJ/mole	$\Delta H_{ADS\ H2S}$ kJ/mole	$\Delta H_{ADS\ CO}$ kJ/mole
PdCu	-28.6	-70.9	-124.6
Pd_8Cu_7G5 – G5 at surface – On top G5	-21.2	-191.7	-121.5
Pd_8Cu_7G5 – G5 at surface – Next to G5	-13.2	-151.5	-108.8
Pd_8Cu_7G5 – G5 subsurface – Near G5	-21.7	-55.1	-96.6
Pd_8Cu_7G5 – G5 subsurface – Away from G5	-20.2	-62.2	-115.9

2.2 Water Gas Shift Catalyst

2.2.1 Catalyst Design and Synthesis

Three rounds of water gas shift (WGS) catalyst synthesis took place as part of this project, each round referred to as a "set". The majority of the catalysts prepared were nominally Pt-Re/$Ce_{0.5}Zr_{0.4}J6_{0.1}O_2$, representing variants of an earlier developed catalyst which demonstrated excellent 400 ºC durability under low pressure water gas shift conditions, as well as tolerance for 2 ppmv H_2S in the feed. However, other compositions outside this range, selected for their potential ability to act as sulfur tolerant water gas shift catalysts, were also synthesized and characterized. In total, nineteen base mixed metal oxides were prepared and metal loaded, yielding fifteen catalysts for test.

The physical property data for all materials tested for WGS activity as part of this project are given in Tables 5–7. Table 5 gives the surface areas and pore size information for the base oxides, which are very high in surface area with small crystallite sizes and large pore diameters. Table 6 provides structural information from X-ray diffraction on the base oxides, giving indication of the phase purity and estimated crystallite diameters. Table 7 gives relevant information as to the metal loadings (Pt and Re), as well as the measured composition of the base oxides.

2.2.1.1 Catalyst Design — Atomistic Modeling

Atomistic modeling was used to guide and interpret both the catalyst synthesis and testing efforts. Due to the computational requirements of the modeling, not all materials were explored in virtual space, but a sufficient number of key materials were chosen to serve as a guide for the catalyst effort. Modeling was performed in two rounds or "sets" in parallel with the synthesis effort.

The first set of catalysts modeled was TiO_2 (anatase), J6-doped TiO_2 and $Ce_{0.5}Zr_{0.4}J6_{0.1}O_2$. The adsorption energies of H_2S, H_2O, and CO on the oxide surfaces were calculated as well as the forward and reverse WGS heats of reaction. In addition, the adsorption energies of H_2S and CO on the oxide surfaces with a monolayer of platinum were calculated. In this first set of modeled catalysts, it was found that the J6-doped TiO_2 was the best in terms of sulfur and CO tolerance with a monolayer of platinum as shown in Table 8 and visually displayed in Figure 11.

Table 5: Surface area and pore size information for three tested sets of WGS catalysts. The surface area per volume of oxide skeletal volume (third column) is determined by multiplying the estimates of oxide skeletal density by the surface area per mass. This allows comparison of activity between catalysts with different oxide densities

Set	Sample Name	Oxide	Surface Area / Mass (m^2/g)	Surface Area / Skeletal V (m^2/cm^3)	Pore Volume (cm^3)	Pore Diameter (nm)
1	STWGS-1-01	$Ce_{0.53}Zr_{0.38}J6_{0.1}O_2$	216	1028	0.28	5.3
1	STWGS-1-02	TiO_2	238	914	0.53	9.1
1	STWGS-1-05	$Ti_{0.8}Ce_{0.2}O_2$	290	1207	0.64	8.8
1	STWGS-1-06	$Ce_{0.333}Zr_{0.333}E4_{0.333}O_2$	246	971	0.39	6.3
1	STWGS-1-07	$Ce_{0.3}Zr_{0.3}E4i_{0.3}J6_{0.1}O_2$	244	1028	0.44	7.2
2	STWGS-2-02	$Ce_{0.33}Zr_{0.33}E4_{0.33}O_2$	291	1590	0.45	6.2
2	STWGS-2-03	$Ce_{0.5}Zr_{0.4}E4_{0.1}O_2$	224	1390	0.30	5.4
2	STWGS-2-04	$Ce_{0.33}Zr_{0.22}E4_{0.40}O_2$	303	1550	0.54	7.1
2	STWGS-2-10	$Ti_{0.9}J6_{0.1}O_2$	334	1480	0.33	4.0
3	STWGS-3-01	$Ce_{0.33}Zr_{0.33}E4_{0.40}O_2$	280		0.44	6.3
3	STWGS-3-02	$Ce_{0.50}Zr_{0.40}J6_{0.10}O_2$	234		0.29	5.0
3	STWGS-3-03	$Ce_{0.50}Zr_{0.40}E4_{0.10}O_2$	240		0.33	5.5
3	STWGS-3-04	$Ce_{0.50}Zr_{0.30}E4_{0.10}J6_{0.1}O_2$	224		0.36	6.4
3	STWGS-3-05	$Ce_{0.50}Zr_{0.40}E4_{0.05}J6_{0.05}O_2$	207		0.28	5.4

Table 6: Structural Information from X-ray diffraction on the three set of WGS catalysts tested.

Set	Sample Name	Oxide	Target Phase	Phase (determined by X-ray diffraction)	Crystal Size / nm
1	STWGS-1-01	$Ce_{0.53}Zr_{0.38}J6_{0.1}O_2$	Cubic	64% cubic, 36% tetragonal Zero J6-oxides	2.5
1	STWGS-1-02	TiO_2	Anatase	>85% anatase, <15% brookite	6.2 / 1.7
1	STWGS-1-05	$Ti_{0.8}Ce_{0.2}O_2$	Cubic	Multi-phase (TiO_2, CeO_2, Ce_2TiO_5, Ce_2TiO_7)	N/A
1	STWGS-1-06	$Ce_{0.333}Zr_{0.333}E4_{0.333}O_2$	Cubic	70% cubic, 21% tetragonal	2.4
1	STWGS-1-07	$Ce_{0.3}Zr_{0.3}E4_{0.3}J6_{0.1}O_2$	Cubic	100% cubic	2.0
2	STWGS-2-02	$Ce_{0.33}Zr_{0.33}E4_{0.33}O_2$	Cubic	96% tetragonal, 4% cubic	2.8 / 5.7
2	STWGS-2-03	$Ce_{0.5}Zr_{0.4}E4_{0.1}O_2$	Cubic	95% tetragonal, 6% cubic	3.0 / 4.7
2	STWGS-2-04	$Ce_{0.33}Zr_{0.22}E4_{0.40}O_2$	Cubic	90% tetragonal, 10% cubic	2.7 / 3.9
2	STWGS-2-10	$Ti_{0.9}J6_{0.1}O_2$	Anatase	65% anatase, 33% brookite, 2% $Ti_{0.5}J6_{0.46}O_2$	4.4 / 3.3
3	STWGS-3-01	$Ce_{0.33}Zr_{0.33}E4_{0.40}O_2$	Cubic	100% cubic	1.6
3	STWGS-3-02	$Ce_{0.50}Zr_{0.40}J6_{0.10}O_2$	Cubic	70% cubic, 30% tetragonal	2.1 / 2.2
3	STWGS-3-03	$Ce_{0.50}Zr_{0.40}E4_{0.10}O_2$	Cubic	75% cubic, 25% tetragonal	2.2 / 2.2
3	STWGS-3-04	$Ce_{0.50}Zr_{0.30}E4_{0.10}J6_{0.1}O_2$	Cubic	70% cubic, 30% tetragonal	2.4 / 3.0
3	STWGS-3-05	$Ce_{0.50}Zr_{0.40}E4_{0.05}J6_{0.05}O_2$	Cubic	74% cubic, 26% tetragonal	2.4 / 1.9

Table 7: Elemental analysis confirming metal loadings and oxide compositions for the three sets of WGS catalysts tested.

Set	Sample Name	Composition (by synthesis)	Composition (by EDAX analysis)	Target Pt wt%	Achieved Pt wt%	Re loaded wt%
1	STWGS-1-01	$Ce_{0.53}Zr_{0.38}J6_{0.1}O_2$	$Ce_{0.54}Zr_{0.37}J6_{0.09}O_2$	2.0	2.09	1.045
1	STWGS-1-02	TiO_2	TiO_2	2.0	0.60	0.30
1	STWGS-1-05	$Ti_{0.8}Ce_{0.2}O_2$	$Ti_{0.88}Ce_{0.12}O_2$	2.0	2.11	1.055
1	STWGS-1-06	$Ce_{0.333}Zr_{0.333}E4_{0.333}O_2$	$Ce_{0.36}Zr_{0.32}E4_{0.33}O_2$	2.0	1.97	0.985
1	STWGS-1-07	$Ce_{0.3}Zr_{0.3}E4_{0.3}J6_{0.1}O_2$	$Ce_{0.32}Zr_{0.28}E4_{0.31}J6_{0..09}O_2$	2.0	1.74	0.87
2	STWGS-2-02	$Ce_{0.33}Zr_{0.33}E4_{0.33}O_2$	$Ce_{0.36}Zr_{0.33}E4_{0.31}O_2$	2.0	3.45 (a), 3.11 (b)	1.75 (a), 1.62 (b)
2	STWGS-2-03	$Ce_{0.5}Zr_{0.4}E4_{0.1}O_2$	$Ce_{0.52}Zr_{0.39}E4_{0.09}O_2$	2.0	2.77 (a), 2.30 (b)	1.44 (a), 1.18 (b)
2	STWGS-2-04	$Ce_{0.33}Zr_{0.22}E4_{0.40}O_2$	$Ce_{0.36}Zr_{0.22}E4_{0.42}O_2$	2.0	3.65 (a), 3.36 (b)	1.84 (a), 1.73 (b)
2	STWGS-2-10	$Ti_{0.9}J6_{0.1}O_2$		2.0	3.56	1.83
3	STWGS-3-01	$Ce_{0.33}Zr_{0.33}E4_{0.40}O_2$		2.0	1.44	0.72
3	STWGS-3-02	$Ce_{0.50}Zr_{0.40}J6_{0.10}O_2$		2.0	0.85	0.45
3	STWGS-3-03	$Ce_{0.50}Zr_{0.40}E4_{0.10}O_2$		2.0	0.77	0.39
3	STWGS-3-04	$Ce_{0.50}Zr_{0.30}E4_{0.10}J6_{0.1}O_2$		2.0	1.38	0.69
3	STWGS-3-05	$Ce_{0.50}Zr_{0.30}E4_{0.05}J6_{0.05}O_2$		2.0	1.83	0.92

(a) first metal loading attempt, (b) second metal loading attempt

Based on the results from the first set of catalysts and experimental testing, a second set of catalyst surrogates was chosen for the modeling study. The second set of model catalysts consisted of subsurface J6-doped TiO_2, $Ce_{0.5}Zr_{0.4}E4_{0.1}O_2$, rutile TiO_2, and $Ce_{0.33}Zr_{0.33}E4_{0.33}O_2$. The results, given in Table 9, indicate that the $Ce_{0.33}Zr_{0.33}E4_{0.33}O_2$ is the best candidate as it has the highest CO and H_2S tolerance both with (Table 8) and without (Table 9) a Pt monolayer. This prediction agrees well with the experimental results, where the catalysts with that oxide composition were shown to be among the best materials.

Table 8: Atomistic modeling predictions of the adsorption binding energies of CO and H_2S on Pt monolayers on various oxide supports.

	Binding Energy (eV)	
	CO	H_2S
TiO_2 Anatase + Pt ML	-1.67	-2.37
$Ti_{0.96}J6_{0.04}O_2$ + Pt ML	-0.97	-2.02
$Ce_{0.5}Zr_{0.4}J6_{0.1}O_2$ +Pt ML	-1.74	-3.66
$Ce_{0.33}Zr_{0.33}E43_{0.33}O_2$+PtML	-0.32	-1.84

Table 9: Atomistic modeling predictions of the adsorption binding energies of CO, H_2O, and H_2S on various oxide supports.

	Binding Energy (eV)			Heat of Reaction(kJ/mol)	
	CO	H_2O	H_2S	$CO + 1/2\ O_2 \rightarrow CO_2 + 2e^-$	$H_2O + 2e^- \rightarrow H_2 + 1/2\ O_2$
1st Set of Models					
TiO_2 Anatase	-0.32	-0.64	-1.93	108.69	-176.91
$Ti_{0.96}J6_{0.04}O_2$	-0.85	-0.79	-2.17	114.29	-182.51
$Ce_{0.5}Zr_{0.4}J6_{0.1}O_2$	-0.63	-0.74	-2.14	149.78	-217.85
2nd Set of Models					
$Ti_{0.96}J6_{0.04}O_2$ (subsur-face dopant)	-0.34	-0.72	-2.09	158.61	-226.82
$Ce_{0.5}Zr_{0.4}E4_{0.1}O_2$	≈-0.3	-1.01	-2.43	146.97	-223.09
TiO_2 Rutile	-0.09	-1.16	-0.90	194.30	-253.98
$Ce_{0.33}Zr_{0.33}E4_{0.33}O_2$	-0.01	-0.83	-0.29	183.46	-252.22

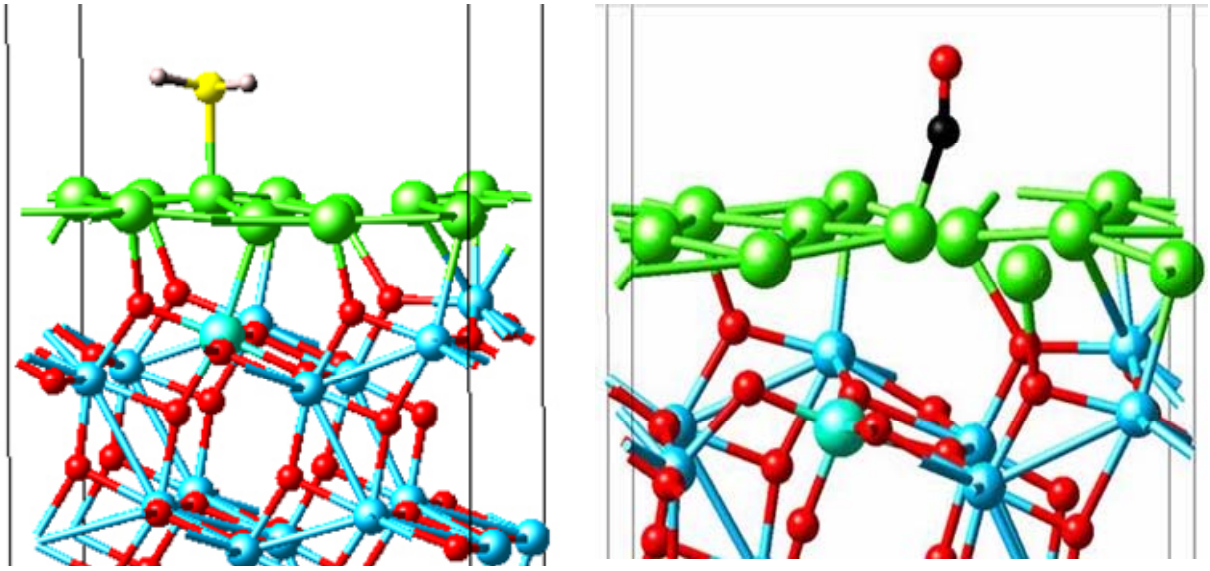

H_2S/Pt_{1ML}/J6-Doped TiO_2 Anatase(101)
Binding Energy: -2.02 eV/H_2S

CO/Pt_{1ML}/J6-Doped TiO_2 Anatase(101)
Binding Energy: -0.97 eV/CO

Figure 11: Atomistic modeling of the adsorption of H_2S and CO onto a Pt monolayer supported by J6-doped TiO_2.

2.2.1.2 Preparation of First Catalyst Set

For the first reactor campaign, a total of five mixed metal oxide catalysts were prepared: (1) $Ce_{0.53}Zr_{0.38}J6_{0.1}O_2$, (2) TiO_2, (3) $Ti_{0.8}Ce_{0.2}O_2$, (4) $Ce_{0.333}Zr_{0.333}E4_{0.333}O_2$ and (5) $Ce_{0.3}Zr_{0.3}E4_{0.3}J6_{0.1}O_2$. The first catalyst composition, $Ce_{0.53}Zr_{0.38}J6_{0.1}O_2$, represents a direct repeat of a catalyst known to demonstrate sulfur tolerance at low pressures. Note that J6 is a proprietary dopant. The second catalyst composition, TiO_2, was selected because titanium is highly refractory compared to cerium and potentially could provide more active participation in the water gas shift reaction at high temperatures. Furthermore, based on the atomistic modeling results, titanium could enhance sulfur tolerance. The third composition selected, $Ti_{0.8}Ce_{0.2}O_2$, represents a mixture of the preferred constituent, cerium, with titanium to see if there were useful interactions. The fourth composition selected, $Ce_{0.333}Zr_{0.333}E4_{0.333}O_2$, represents a mixture of the preferred WGS constituents, cerium and zirconium, with a proprietary dopant E4 in an even distribution. Finally the fifth composition selected for testing, $Ce_{0.3}Zr_{0.3}E4_{0.3}J6_{0.1}O_2$, was the most complex, representing an oxide with an even distribution of the preferred constituents and doped with the proprietary dopants J6 and E4.

All five oxides were synthesized using a proprietary urea homogeneous coprecipitation method using either a metal nitrate or metal chloride salt as one of the starting materials. They were then converted into the final catalyst material by first metal loading them with platinum using a proprietary ion-exchange technique and then with rhenium using a proprietary reduction/decomposition technique. All of the oxides were targeted to give small crystallite size (~ 2 nm) high surface area (>180 m^2/g), a large pore structure (>5 nm pore diameter), and a cubic phase (except for composition #2 which was targeted to form the anatase phase). For the most part, this goal was satisfied. One exception to this was the phase separation of the $Ti_{0.8}Ce_{0.2}O_2$ catalyst (composition #3), which was postulated to be due to an unfavorable atomic size mismatch between cerium and titanium.

All of the oxides were targeted to be loaded with 2 wt% platinum. Based on the actual achieved loading, a 2:1 ratio of Pt:Re was then targeted. For the most part, this goal was achieved except for the catalyst composition #2, TiO_2, which yielded a very low loading of platinum.

2.2.1.3 Preparation of Second Catalyst Set

For the second reactor campaign, a total of nine mixed metal oxide catalysts were prepared with four materials down-selected for catalyst testing to be compared with a repeat run of $Ce_{0.33}Zr_{0.33}E4_{0.33}O_2$ (STWGS6). These compositions were selected based on the test results from the first round of catalyst materials as well as input from atomistic modeling. The first oxide material, $Ce_{0.33}Zr_{0.33}E4_{0.33}O_2$, was a repeat of the fourth catalyst tested as part of round one (STWGS6). This oxide, once metal loaded, gave the highest aged 1.8 atm activity in the presence of sulfur. Two other oxide compositions, $Ce_{0.50}Zr_{0.40}E4_{0.1}O_2$ and $Ce_{0.50}Zr_{0.40}J6_{0.1}O_2$, respectively, represented variants upon the first catalyst tested in the second set. Another catalyst, which was “E4-rich” compared with the STWGS6 type catalyst, was chosen based on the desire to balance the ratio of atomic

radii of all cations. Specifically, the Ce/(Zr + E4) was held constant between the two materials. The final oxide composition, $Ti_{0.9}J6_{0.1}O_2$, contained the same dopant, J6, as in the $Ce_{0.50}Zr_{0.40}J6_{0.1}O_2$ catalyst, however in a titania, not ceria-zirconia, based structure.

All oxide materials were prepared using the methods described above. Similar to the first round of materials synthesized, these oxides were very high in surface area with small crystallite sizes and large pore diameters. Once the oxides were obtained, platinum and then rhenium were then loaded on the surface using the methods described above.

The target platinum loading was again 2.0 weight percent. During the first round the Pt loading, however, the proprietary ion-exchange technique was not compatible with TiO_2 and consequently the Pt loading was low. A modified proprietary ion-exchange technique was therefore used in the second round. The target platinum (Pt)/rhenium (Re) ratio was again 2:1. The rhenium was loaded via the proprietary reduction/ decomposition technique described above. The platinum loadings that were achieved were, for the first attempt, all higher than that targeted (e.g., closer to 3 weight percent). The loading step was therefore repeated, using second portions from the same oxide powder batches and changing the process parameters to be less aggressive. The resulting weight percents were lower, however still high compared to the target. For testing for WGS activity, when there were two choices of materials available, the one with the platinum loading closer to 2.0% was selected.

2.2.1.4 Preparation of Third Catalyst Set

For the third reactor campaign, a total of five mixed metal oxide catalysts were prepared: (1) $Ce_{0.33}Zr_{0.33}E4_{0.4}O_2$, (2) $Ce_{0.50}Zr_{0.40}J6_{0.10}O_2$, (3) $Ce_{0.50}Zr_{0.40}E4_{0.1}O_2$, (4) $Ce_{0.50}Zr_{0.30}E4_{0.10}J6_{0.1}O_2$, and (5) $Ce_{0.50}Zr_{0.40}E4_{0.05}J6_{0.05}O_2$. These compositions were based on test results obtained from the second set of catalysts tested, which gave indication that the most active catalysts under the prescribed conditions (1atm pressure, 10 ppm level sulfur) were mixed cerium zirconium oxides containing, as either an alloying or doping constituent, E4 or J6. Based on this observation, the compositions of the last set of catalysts were selected to give insight as to the best distribution between of these two constituents or, alternatively, to determine which constituent was better if used alone.

2.2.2 Catalyst Testing

The WGS activity measurements were conducted in a catalyst screening rig used to evaluate five different catalysts simultaneously under identical inlet gas compositions and space velocities. Quantities (0.150.3 g) of the 80-120 mesh catalysts loaded with noble metal, were uniformly blended with 5 cm^3, or 9.4 g, of +40-mesh Strem Chemical alpha alumina granules and charged into a 0.5-in O.D,. 316L Stainless Steel reactor tube with 0.049-in walls with a 0.402-in I.D. equipped with a 0.125-in O.D. axial thermowell. The net cross sectional area of the reactors was 0.74 cm^2. The catalyst charge was separated from a bottom frit by a 5.25-in length of 10-mesh alundum granules and a thin wad of borosilicate glass wool. The catalyst and 40-mesh alumina diluent bed together was 3.0-in long, and topped with a thin wad of borosilicate glass, above which was loaded about 5-in more of 10-mesh alundum granules.

As this was a down flow reactor, the 5-in top section served to preheat the reaction gas mixture to reaction temperature before it contacted the dilute catalyst. This was confirmed during the initial heating and reduction by the internal, 0.0625-in K-type thermocouple in the internal, axial thermowell. The 0.5-in O.D. reactor tube was placed inside a tight fitting aluminum block to minimize axial temperature gradients, and no axial thermal gradient was found at 320 °C under 20% hydrogen/80% nitrogen flowing at 2.6 standard liters per minute (SLPM).

Figure 12 presents a schematic of the fully automated multi-reactor rig used in these experiments. The experiments were conducted at a space velocity of ~200,000 h^{-1} and the temperature of the catalyst bed was measured by the K-type thermocouple in the axial thermowell. The flow of UHP grade compressed gases N_2, H_2, CO, CO_2, and H_2S/H_2 were controlled by Brooks Flow Controllers (Model 5850E) and combined at ambient conditions in a mixing manifold. The mixed gases were then sent through a compressor that enabled variation of reactor pressures from 1–42 atm. De-ionized water was fed to a steam generator that operated at approximately 270 °C. The steam generator was coated on the inside with Silcosteel® coating to prevent coke formation. The mixed dry gases were then contacted with the steam in the steam generator to obtain the final gas mixture. This hot gas mix was distributed using Swagelock needle valves to each individual reactor.

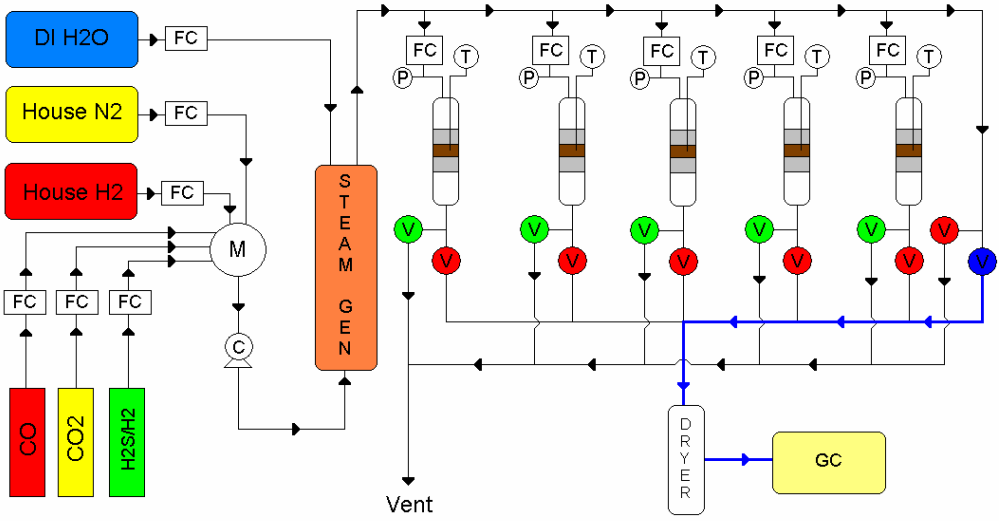

Figure 12: Catalyst testing rig schematic.

The generic experimental protocol used had the following features:

a) Preliminary drying of the gases in nitrogen flow at 150 °C.
b) Reduction of the catalyst in 8%-40% hydrogen with a balance of N_2 in the 240 °C to 330 °C range.

c) Stepwise addition of steam from a concentration of 0% to 33% with 30% H_2 and balance N_2 at 320 °C.
d) Determination of the WGS activity at various simulated coal gas reformate compositions with temperatures varied from 400 °C to 300 °C at 1 atm without the H_2S feed.
e) Determination of the sulfur free WGS kinetics by varying gas compositions at various pressures.
f) Determination of activity at various pressures and sulfur introduced as H_2S at approximately 100 ppm of overall mixture.

The inlet and exit gases from the system were analyzed using a Varian GC equipped with three detectors (one FID and two TCDs), a methanizer, and six separation columns. The first two columns (61 cm and 92 cm Haysep DB 80/100 mesh columns, 1 mm ID), and the first TCD (H_2 carrier) were used to detect N_2, Ar and CO_2. The vent from the second column was connected through a valve to two other separation columns (both 183 cm Mol Sieve 5A 80/100 mesh columns, 1 mm ID). These columns were used to separate CO, CO_2, and CH_4. The effluent from these columns was fed through the methanizer to the FID for detection. The final two columns (61 cm and 122 cm Haysep DB 80/100 mesh columns, 1 mm ID) and a second TCD (N_2 carrier gas) were used to detect H_2. The feed gas composition measured between product gas composition measurements was used in the determination of CO conversion. The turnover numbers presented in this report were calculated using the expression
TOR = (% CO converted)×(Flow rate in mol/s)/(Total amount of metal loaded in moles).

2.2.2.1 Activity and Kinetics Results

The first two sets of catalysts were primarily put through testing at atmospheric conditions and slightly elevated pressures to identify promising candidates for the elevated pressure kinetics and aging experiments. In addition, testing during the first two sets resulted in the modification of the testing rig to its final form, including the Silcosteel®-coated steam generator to prevent coking that occurred earlier in the project. Figure 13 shows turnover rates obtained for the first set of catalysts where the catalyst composition was varied by primarily changing the dopant type between, E4 and J6. STWGS1 and STWGS6 are a direct comparison of the CeZrJ6 and CeZrE4 compositions, respectively. The E4-doped catalysts showed greater activity than the J6-doped catalysts and these results suggested focusing the next round of synthesis around optimization of the J6 compositions.

Figure 14 presents the activity results from the second batch of catalysts that were tested at 400 °C and with a gas composition of 7.2% CO, 7.8% CO_2, 6% H_2, and 39.2% H_2O. Data at 80, 100, and 120 hours are each reported at 1 atm pressure with the sulfur concentration at 100 h at a 10-ppm level. The oxide compositions, $Ce_{0.5}Zr_{0.4}E4_{0.1}$ (203B) and $Ce_{0.33}Zr_{0.33}E4_{0.33}$ (202B) seemed to both have adequate performance with small levels of sulfur.

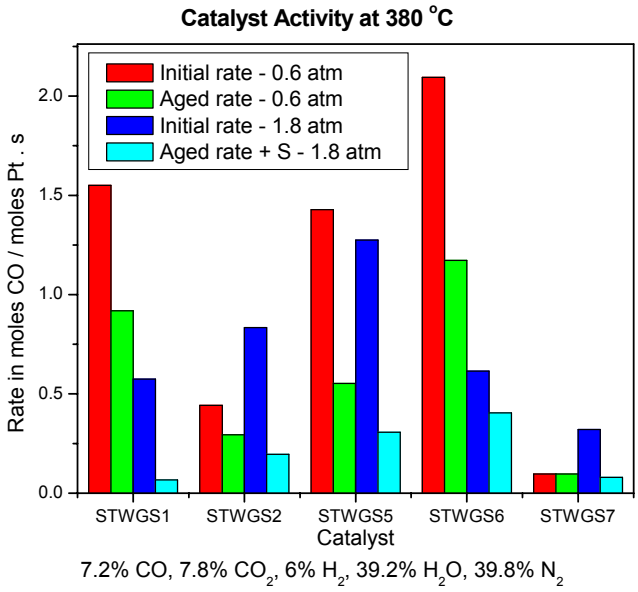

Figure 13: Testing results for the first set of catalysts.

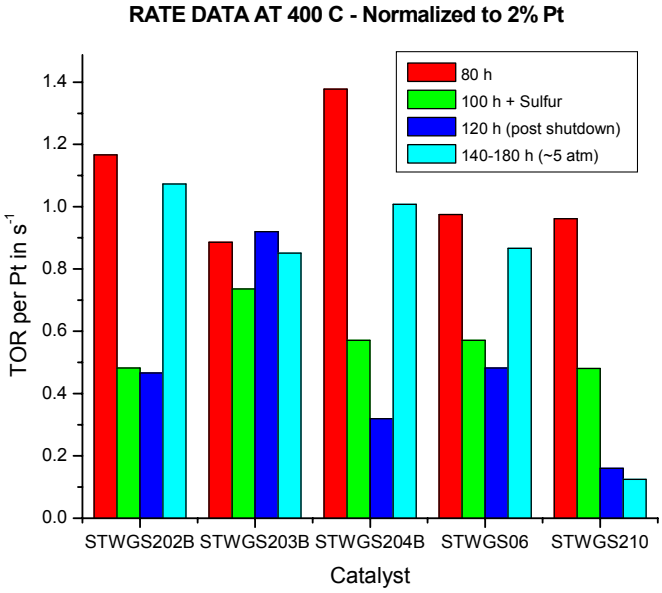

Figure14: Testing results for the second set of catalysts.

The 120 h uncontrolled shutdown condition occurred when gas flow was suddenly interrupted and the reactors went through a cool down in the presence of dry gas (no steam). Less robust catalysts might be poisoned by sulfur or by coke formation under these conditions. However, the optimized compositions seemed to be resilient under these conditions as well. This was confirmed in a third round of testing, where both the $Ce_{0.33}Zr_{0.33}Ti_{0.33}O_2$ and $Ce_{0.5}Zr_{0.4}Ti_{0.1}$ compositions were chosen for long term durability and high pressure/high sulfur runs.

Integral reactor kinetics experiments were performed for the preferred catalyst compositions after they were aged in a 120–220-h time range and the rates were fit to the kinetic model:

$$\text{Rate} = A*\exp(-Ea/RT) * [CO]^a * [H_2O]^b * [CO_2]^c * [H_2]^d * (1-\beta) \quad (5)$$

where: $\beta = ([CO_2] * [H_2]) / (K*[CO]*[H_2O])$ is the approach to equilibrium, A = Pre-exponential factor, Ea = Activation energy, T = Temperature, a = CO reaction order, b = H_2O reaction order, c = CO_2 reaction order, d = H_2 reaction order.

Table 10 presents a summary of the calculated kinetic rate parameters at 42 atm for the two down-selected catalysts. Data for kinetics obtained for the $Ce_{0.33}Zr_{0.33}E4_{0.33}O_2$ composition at atmospheric pressure are also included. The results suggest that increasing pressure has the impact of decreasing CO orders while further increasing the negative dependency of the reaction rates on the H_2 order. The latter is of particular significance because it illustrates the need for incorporating the catalyst within a membrane separator to facilitate separation that will limit the negative impact of H_2 order on the rate.

Table 10**:** WGS kinetic parameters for down-selected catalysts

Catalyst	CO order	H_2O order	CO_2 order	H_2 order	Ea (kJ/mol)
$Ce_{0.33}Zr_{0.33}E4_{0.33}O_2$ (1 atm)	0.80±0.20	0.68±0.45	-0.41±0.28	-0.53±0.31	92±11
$Ce_{0.50}Zr_{0.40}E4_{0.10}O_2$ (42 atm)	0.24±0.01	0.0	0.0	-0.31±0.01	53±11
$Ce_{0.33}Zr_{0.33}E4_{0.33}O_2$ (42 atm)	0.1±0.3	0.0	-0.3±0.6	-0.9±0.3	55±8

2.2.2.2 Durability Results

Figure 15 shows the results from the durability runs conducted on the down-selected catalysts with and without sulfur. The plot on the left indicates that catalyst deactivation rates with and without sulfur followed the same trend suggesting that there was limited deactivation contribution from the sulfur. It is proposed that certain catalyst poisoning mechanisms related to oxide deactivation such as the formation of carbonate or formate species could be responsible for much of the deactivation observed at these conditions. Combining the catalyst with a hydrogen separator might prevent these poisoning mechanisms by enhancing overall water gas shift rates, as the kinetic rates of both materials depend inversely on the hydrogen concentration.

The plot on the right of Figure 15 suggests that the best catalyst, Pt-Re/$Ce_{0.333}Zr_{0.333}E4_{0.333}O_2$, will not meet a projected five year lifetime turnover rates of

0.5 s^{-1}, despite a high initial rate. Fundamental work (through atomistic modeling and in situ spectroscopy experiments) to understand deactivation mechanisms should be undertaken as a future research project to further optimize the catalyst. Additional catalyst testing should also be performed under different pressures, space velocities, amounts of catalyst, and gas compositions to further determine the cause of catalyst deactivation.

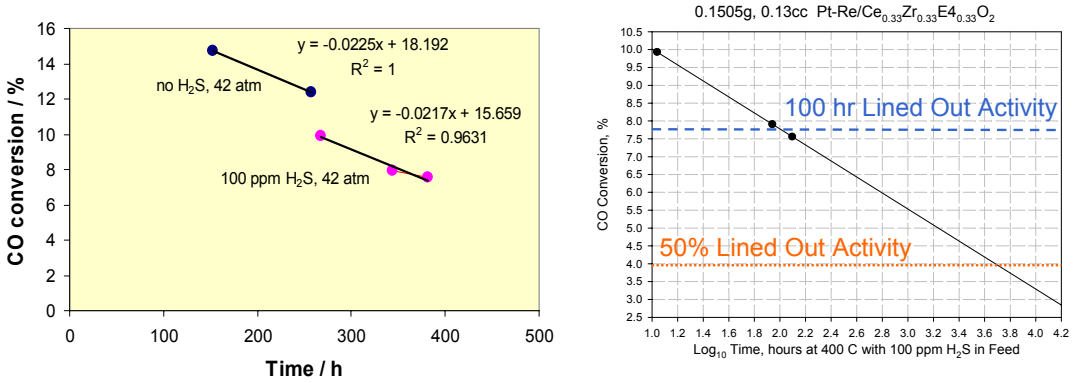

Figure 15: Durability results for the best catalyst from this project, Pt-Re/$Ce_{0.333}Zr_{0.333}E4_{0.333}O_2$.

3 Conclusion

This project successfully identified a suitable PdCu tri-metallic alloy membrane with high stability and commercially relevant hydrogen permeation in the presence of trace amounts of carbon monoxide and sulfur. The alloy composition, $Pd_{0.47}Cu_{0.52}G5_{0.01}$, was selected based solely on atomistic and thermodynamic modeling. To achieve the DOE's goals of identifying a suitable Pd alloy membrane that can withstand the challenges of coal gasifier syngas, this alloy's performance needs to be verified experimentally. The construction and experimental study of a membrane separator based on this alloy is planned as part of another project for the DOE, DE-FC26-07NT43055.

The project also identified WGS catalyst compositions that can withstand sulfur in high concentrations and at high pressures. However, from the limited durability testing it appears that the best catalyst, Pt-Re/$Ce_{0.333}Zr_{0.333}E4_{0.333}O_2$, is unable to maintain a long operating life at space velocities of 200,000 h^{-1}. The reasons for the low durability do not appear to be related to the high concentrations of H_2S, but rather due to the high operating pressure and the influence the pressure has on the WGS reaction. Based on the strong inverse dependence of the catalyst kinetics on hydrogen pressure, operation of this type of catalyst within a hydrogen separation process, such as a $Pd_{0.47}Cu_{0.52}G5_{0.01}$ alloy membrane, should boost activity. Reduction in the operating space velocity, and thus an increase in the amount of catalyst for a given flow rate, may also improve catalyst durability. Additional work should be performed to investigate the causes of catalyst deactivation at high pressures as well as to estimate the amount of catalyst required to maintain life for DOE's coal gasification applications.

4 References

[1] S. M. Opalka, W. Huang, D. Wang, T. B. Flanagan, O. M. Løvvik, S. C. Emerson, Y. She, and T. H. Vanderspurt, "Hydrogen interactions with the PdCu ordered B2 alloy," J. Alloys Compd., in press, doi:10.1016/j.jallcom.2007.01.130.

[2] W. Huang, S. M. Opalka, D. Wang, and T. B. Flanagan, CALPHAD, 31(3) (2007) 315.

[3] D. E. Jiang and E. A. Carter, Phys. Rev. B 70 (2004) 064102.

[4] J. Piper, J. Appl. Phys. 37 (1966) 715.

[5] J. Völkl, G. Alefeld, "Diffusion of Hydrogen in Metals" in "Hydrogen in Metals, Vol.I"(Vol. 28 of topics in Applied Physics), G. Alefeld and J. Völkl, Eds., Springer Verlag, Berlin (1978) 321.

[6] J. Shu, B. P. A. Grandjean, A. Van Neste, S. Kaliaguine, Can. J. Chem. Eng. 69 (1991) 1036.

[7] The hydrogen partial molar volume increase has been determined to be 1.77 x 10^{-24} m^3 /mol H from a number of binary Pd alloys. This relationship was first reported by B. Baranowski, S. Majchrzak, and T. B. Flanagan, J. Phys. F., 1 (1971) 258.

[8] P. Kamakoti, B. D. Morreale, M. V. Ciocco, B. H. Howard, R. P. Killmeyer, A. V. Cugini, D. S. Sholl, Science 307 (2005) 569.

[9] Y. H. Ma, E. E. Engwall, and I. P. Mardilovich, Preprints of Symposia - American Chemical Society, Division of Fuel Chemistry 48(1) (2003) 333.

[10] D. R. Alfonso, A. V. Cugini, D. Sorescu, Prepr. Pap.-Am. Chem. Soc., Div. Fuel Chem. 48(2) (2003) 512.

[11] D. R. Alfonso, A. V. Cugini, D. S. Sholl, Surf. Sci. 546(1) (2003) 12.